No-Reference Sharpness Assessment of Camera-Shaken Images by Analysis of Spectral Structure

Taegeun Oh, Jincheol Park, Kalpana Seshadrinathan, *Member, IEEE*, Sanghoon Lee, *Senior Member, IEEE*, and Alan Conrad Bovik, *Fellow, IEEE*

***Abstract*— The tremendous explosion of image-, video-, and audio-enabled mobile devices, such as tablets and smart-phones in recent years, has led to an associated dramatic increase in the volume of captured and distributed multimedia content. In particular, the number of digital photographs being captured annually is approaching 100 billion in just the U.S. These pictures are increasingly being acquired by inexperienced, casual users under highly diverse conditions leading to a plethora of distortions, including blur induced by camera shake. In order to be able to automatically detect, correct, or cull images impaired by shake-induced blur, it is necessary to develop distortion models specific to and suitable for assessing the sharpness of camera-shaken images. Toward this goal, we have developed a no-reference framework for automatically predicting the perceptual quality of camera-shaken images based on their spectral statistics. Two kinds of features are defined that capture blur induced by camera shake. One is a directional feature, which measures the variation of the image spectrum across orientations. The second feature captures the shape, area, and orientation of the spectral contours of camera shaken images. We demonstrate the performance of an algorithm derived from these features on new and existing databases of images distorted by camera shake.**

***Index Terms*— Image sharpness assessment (ISA), image quality sharpness (IQA), motion blur, camera-shaken image, no-reference, spectral structure.**

I. Introduction

RECENTLY, hand-held cameras installed in mobile devices such as tablets and smart-phones have become pervasive, making the acquisition and distribution of images highly convenient. However, when images are acquired in a casual manner, or under difficult conditions, or by an unskilled user, the quality of the images so obtained is often unacceptable due to distortions occurring during capture such as low-light noise, focal blur [1], [2] and camera shake induced blur [3]–[5]. In particular, blur induced by camera shake is a common and severe impairment that occurs in poorly controlled situations, e.g., without a tripod. Optical image stabilization techniques attempt to compensate for camera shake, but this technology is imperfect, is not yet available in many cell phone cameras and does not eliminate blur induced by camera shake [6], [7]. This makes the development of an automated device for detecting and assessing blur from camera shake an important goal. Success in this direction will help make it possible to monitor and control the quality of images as they are being acquired by handheld digital cameras. Moreover, such an algorithm could be used to cull existing photographs, or as a source of perceptually optimized feedback for restoring image sharpness.

No-reference image quality assessment models have been previously proposed that can predict the perceptual quality or sharpness of an image by predicting distortions such as blocking, blur, channel distortion, etc. Blur is a particularly complex and critical factor influencing the perceptual quality of images, which can occur during all stages of capture [1], [8], compression [9]–[11] and transmission [12]–[14]. The problem is complicated by desirable blur, viz., consciously not selected by the photographer to be "in focus" and hence falling outside of the camera's depth of field (DoF) [15]. Numerous techniques have been studied to measure the sharpness of images, which may be conveniently divided into two broad categories: 1) edge-based methods, and 2) spectral-based methods. Edge-based methods generally seek to measure the spread of edges in the image under the assumption that there is at least one edge in the image and that the width of edges increases when the image is blurred [1], [16]–[20]. Edge width is commonly measured by modeling blurred edges as integrals of Gaussian functions [16], [17] or by estimating the distance between the start and end positions of the edge [1], [18]–[20]. Spectral-based methods measure the spectral distribution under the assumption that edges and textured regions promote high frequency energy [21]–[23]. These methods typically estimate sharpness in the discrete fourier transform (DFT) or discrete cosine transform (DCT) domain by analyzing the histogram or other statistics of the spectral coefficients [21]–[23].

A variety of recent quality assessment algorithms adopt a learning approach to capture image distortion characteristics.

Manuscript received December 4, 2013; revised May 1, 2014 and August 4, 2014; accepted October 12, 2014. Date of publication October 23, 2014; date of current version November 12, 2014. This work was supported by the Ministry of Science, ICT and Future Planning, Korea, through the ICT Research and Development Program in 2014. The associate editor coordinating the review of this manuscript and approving it for publication was Prof. Damon M. Chandler. *(Corresponding author: Sanghoon Lee.)*

T. Oh, J. Park, and S. Lee are with the Department of Electrical and Electronic Engineering, Yonsei University, Seoul 120-749, Korea (e-mail: tgoh27@yonsei.ac.kr; dewofdawn@yonsei.ac.kr; slee@yonsei.ac.kr).

K. Seshadrinathan is with Intel Labs, Intel Corporation, Chandler, AZ 85226 USA (e-mail: kalpana.seshadrinathan@intel.com).

A. C. Bovik is with the Laboratory for Image and Video Engineering, Department of Electrical and Computer Engineering, University of Texas at Austin, Austin, TX 78712 USA (e-mail: bovik@ece.utexas.edu).

Color versions of one or more of the figures in this paper are available online at http://ieeexplore.ieee.org.

Digital Object Identifier 10.1109/TIP.2014.2364925

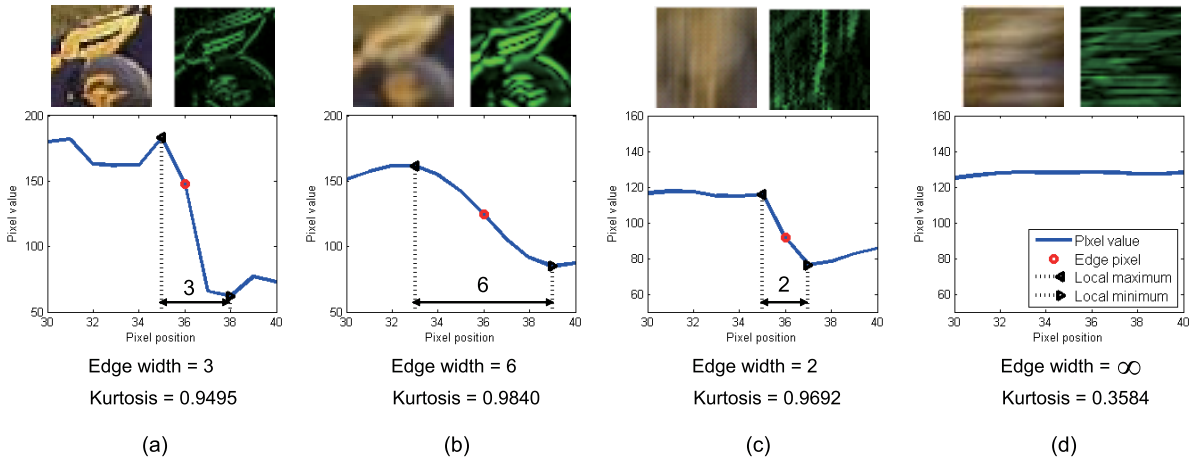

Fig. 1. Limitations of edge-based and spectral sharpness estimation methods. (a) Reference image (top-left), which is a patch of the 30^{th} frame of the *football* sequence, gradient magnitude (top-right), and a plot of luminances (bottom) along a row of the reference image where circles indicate the edge pixels and triangles indicate local extrema. (b) Gaussian blurred version ($\sigma = 2.0$) of (a). (c) Blurred version of (a) obtained by simulating vertical camera movement. (d) Blurred version of (a) obtained by simulating horizontal camera movement.

These algorithms use features derived from natural scene statistics models to learn quality prediction engines [24]–[26]. However, the features used in these models are quite general, suitable for characterizing noise, compression artifacts, and isotropic blurs induced by defocus or compression. While such general purpose blind image quality assessment (IQA) models may also be responsive to blur induced by camera shake, they generally are unable to distinguish it from other distortions or to characterize the nature of the blur.

Likewise, edge and spectral-based sharpness assessment algorithms are usually not designed to measure quality degradations caused by camera shake, instead they are also designed to deal with blur caused by defocus or compression. When an image is blurred by camera shake, the blur severity varies with the direction of camera movement, as opposed to blur from defocus or compression, which tends to be isotropic. Further, camera shake is different from object motion blur, which is created by the presence of independently moving objects in a scene against a static or slower-moving background [8], [27]–[30].

In the following we describe a no-reference model for Image Sharpness Assessment of Camera-shaken images (ISAC) based on analysis of image spectral structure. When there is camera movement, high frequency components are attenuated in a manner that depends on the speed and direction of camera motion. These observations naturally lead us to consider two classes of features that are predictive of the amount of perceived blur in a camera shaken image.

- Directional features : These capture the severity of camera shake induced blur by measuring the variance and energy of the image spectrum along different orientations, which serve to capture blur strength as a function of direction [31]–[35]. In particular, the directional features are obtained by calculating the mean, coefficient of variation (CV) and minimum sharpness of the image spectrum across multiple orientations.
- Shape features : Camera shake asymmetrically modifies the shape of the image spectrum across spatial frequency bands. We model the image spectrum using ellipses and measure the area, eccentricity and orientation of these ellipses to compute spectral shape features.

Finally, we construct a predictive model using support vector regression (SVR) on the directional and shape features. This regression model, which we term ISAC, is used to predict the sharpness of camera-shaken images. In order to verify the performance of ISAC, we constructed a database of camera-shaken images and conducted subjective studies to gather human judgments of the quality of these images. The performance of ISAC is shown to be superior to other image sharpness assessment algorithms on this database. We also evaluated the performance of ISAC on other existing databases of camera shaken images by gathering human judgments of quality of these images and found highly competitive performance.

II. Motivation

Fig. 1 illustrates the failure of existing edge-based and spectral models when predicting blur induced by camera shake in a manner consistent with visual perception. Fig. 1 shows a reference image and distorted images obtained by simulating isotropic defocus blur and blur induced by horizontal and vertical camera movement. We simulated camera movement using a linear motion blur kernel [29], [36] assuming a velocity of 30 pixels along the horizontal and vertical directions respectively.

Edge-based methods [1], [18] that estimate image sharpness by measuring edge widths are unsuitable for measuring blur induced by camera shake. This is illustrated in Fig. 1, where edge boundaries are identified as the local maximum and minimum of a Sobel filtered image patch. Edge width is then calculated using the distance between these boundaries. While edge width increases in the presence of isotropic blur as shown in Fig. 1(b), any change of edge width in camera shaken images depends on the motion direction. In particular, if the edge width is measured in a direction perpendicular to the direction of image motion as illustrated in Fig. 1(c), then camera shake induced blur will produce no measurable effect.

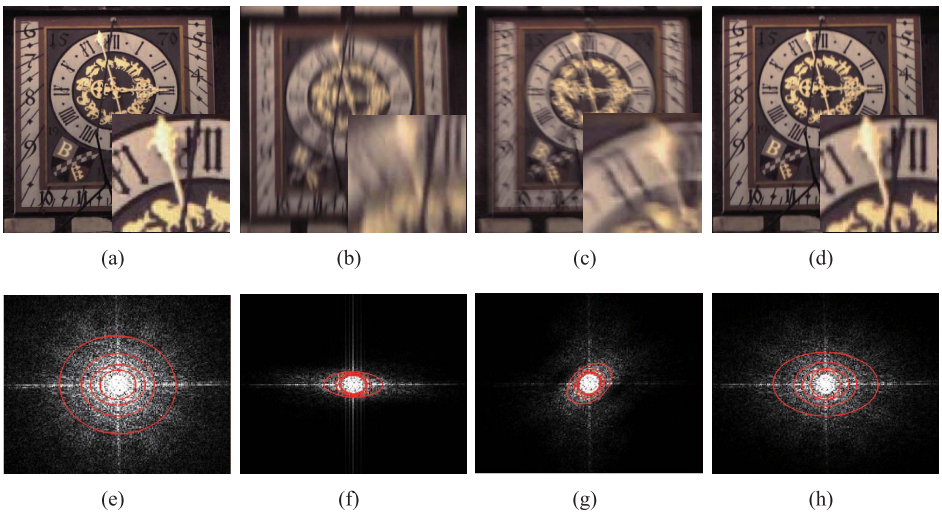

Fig. 2. (a) Natural images. (b) Linear camera-shaken versions of (a). (c) and (d) Complex camera-shaken versions of (a). The bottom-right of each image is a zoomed version of the larger image in each case. (e)–(h) The DFT spectra of (a)-(d), where brighter regions indicate larger DFT magnitude. The ellipsoids are the spectral contours that capture 60%, 70%, 80% and 90% of the energy of the spectrum, respectively.

Spectral kurtosis [23] is a spectral image sharpness assessment method that is also inadequate for measuring blur induced by camera shake. This is illustrated in Fig. 1(d) where the kurtosis of the image is very low despite severe blur due to camera shake.

These limitations of existing blur models clearly illustrate the need for new models to predict blur in camera shake induced images. In Section III, we describe the spectral statistics of camera shaken images that can be utilized to predict perceptual blur of these images.

III. Overview of Proposed Approach

Blur caused by camera shake can be broadly categorized based on the type(s) of camera movement that occurs [4], [37]:

- Linear shake : Caused by linear movement of the camera along a specific direction.
- Complex shake : Caused by complex camera movements arising from the user's hand shaking along multiple directions.

Complex shake is more likely to occur when a user takes a picture and can be approximated using a combination of linear camera shake models.

When linear camera movement degrades the image, high frequency energy along the direction of camera motion is significantly attenuated. The point spread function (PSF) of camera shake induced blur can be expressed as a line mass under the assumption that the relative motion between the camera and the scene occurs at a constant projected velocity V in a direction ϕ [29]:

$$h(x,y) = \begin{cases} \frac{1}{V}, & \text{if } \sqrt{x^2+y^2} \leq \frac{V}{2} \text{ and } \frac{x}{y} = -\tan(\phi); \\ 0, & \text{otherwise,} \end{cases} \quad (1)$$

where (x, y) are the horizontal and vertical pixel coordinates, respectively.

In the DFT domain, camera shake induced blur may be expressed using:

$$H(u,v) = \text{sinc}\,(\pi V \eta) \quad (2)$$

where (u, v) are horizontal and vertical spatial frequency coordinates respectively, $H(u, v)$ is the DFT of $h(x, y)$ and $\eta = u\cos\phi + v\sin\phi$. This formulation can be applied to global space-invariant blur or to local space-varying blur.

Both linear and complex camera motion modify the DFT spectrum of the image along specific directions that depend on the direction of motion. Further, since the motion of the camera occurs as the image is being integrated on the sensor, attenuation of the high frequency components of the DFT spectrum occurs along these directions. We define two types of features that capture these effects by making shape measurements on the image DFT spectrum. First, directionality features capture the degree of orientation of the image DFT that may occur due to camera motion. Secondly, shape features capture the degree of attenuation of higher frequency components of the image due to motion blur.

This directionality of the spectra of camera shaken images is illustrated in Fig. 2, which shows several linear and complex camera-shaken images and their DFT spectra. Complex camera movement is seen to cause higher frequency attenuation in multiple, but not all, directions as illustrated in Fig. 3. Further, perceived blur has been shown to depend on the speed and direction of camera movement [32], [33]. Based on these observations, we define the measure of directional sharpness to be a function of the energy and variance of the image spectrum along multiple directions. We then define three directional features that are predictive of the degree of perceived blur: the average directional sharpness (F_1), the coefficient of variation (CV) of directional sharpness (F_2) and the minimum directional sharpness (F_3) (described in Section IV). We motivate the choice of these three statistics by a few illustrative examples that are shown in Figs. 3 and 4. We explain the rationale behind each feature later.

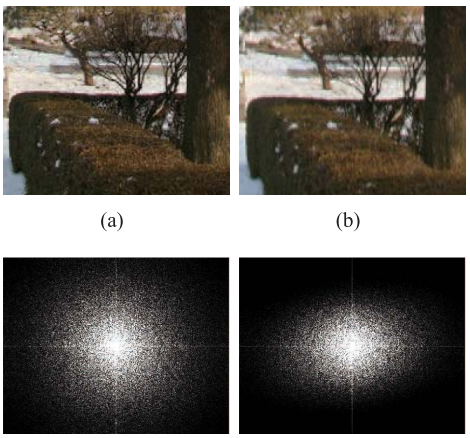

(a) (b) (c) (d)

Fig. 3. Zooms of (a) a natural image and (b) a real complex camera-shaken version of (a). (c) DFT spectra of (a). (d) DFT spectra of (b).

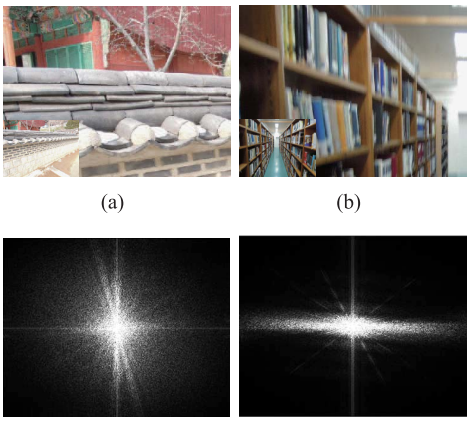

(a) (b) (c) (d)

Fig. 4. Zooms of (a) a natural image and (b) a linear camera-shaken version of (a). The bottom-left of each image is an original version in each image. (c) The DFT spectrum of (a) and the directional statistics described in Section III ($F_1 = 0.3952$, $F_2 = 0.0798$ and $F_3 = 0.4161$). (d) The DFT spectrum of (b) and the directional statistics described in Section III ($F_1 = 0.3831$, $F_2 = 0.4913$ and $F_3 = 0.1630$).

Fig. 3 illustrates how complex camera shake reduces the average directional sharpness of the image spectrum. Fig. 4 shows how the CV and the minimum directional sharpness are indicative of perceptual blur, even in cases where the average directional blur is not discriminative. Depending on the image content, some images could have a relatively high average directional sharpness even in the presence of camera shake. However, the spectral structure will be asymmetrically modified by camera motion. The feature F_2 serves to quantify the variation of directional sharpness across orientations, while F_3 measures the severity of perceptual blur along the camera motion direction.

We also utilize shape features in the spectral domain to quantify perceptual blur. The shape features are based on fitting ellipses to the spectral contours of an image. Fig. 2 shows the fitted ellipses that (in order of increasing size) capture 60%, 70%, 80% and 90% of the image's spectral energy [38]. Observe that the areas of these ellipses increases rapidly on natural images, but the rate of increase is

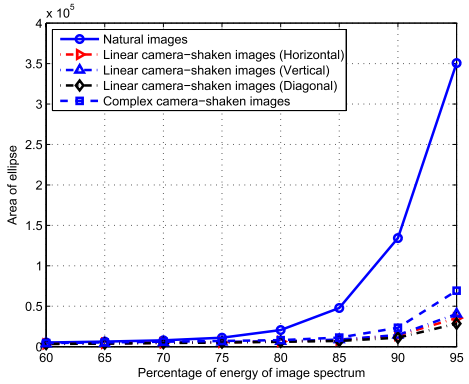

(a)

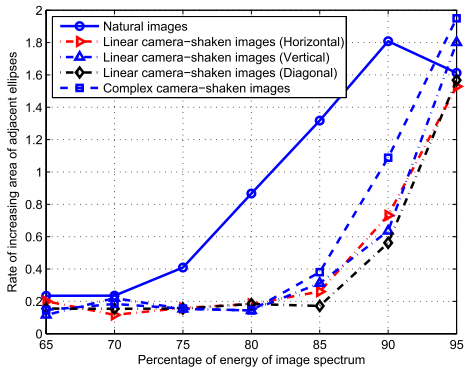

(b)

Fig. 5. (a) Average areas and (b) rate of increase of elliptical area. The ellipses model spectral contours of an image as a function of percentiles of spectral energy.

diminished in the presence of camera shake. This is illustrated in Fig. 5, which plots the average areas of fitted ellipses and the rate of increase of elliptical areas on the Camera-Shaken Images (CSI) database (described in Section V). Further, we observe that the eccentricity and orientation of the ellipses tend to be concentrated within a narrow range on natural images but vary widely on complex camera-shaken images. This is illustrated in Fig. 6, which shows the eccentricity and orientation of fitted ellipses on natural and complex camera-shaken images from the CSI database.

Based on these observations, we also define three spectral shape features that quantify the area, eccentricity and orientation of the fitted ellipses: the rate of increase of elliptical areas (F_4), the sample variance of the spectral eccentricities (F_5) and the spectral orientations (F_6). The details of our model and algorithm for measuring camera shake induced blur are presented in Section IV.

IV. No-Reference Image Sharpness Assessment of Camera-Shaken Images (ISAC)

In this section, we describe in detail the spectral domain directional and shape features that are used in ISAC to measure the degree of camera shake induced blur that may afflict an image being analyzed. We then build a regression model that performs perceptual sharpness estimation by training on these features against recorded human subjective judgments.

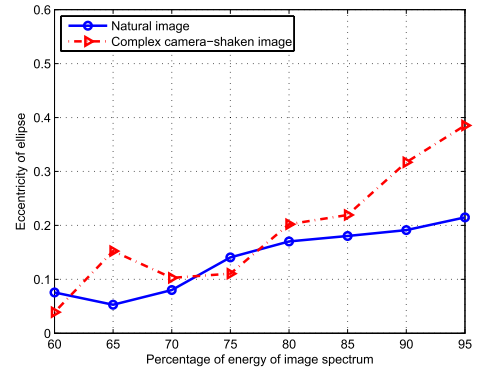

(a)

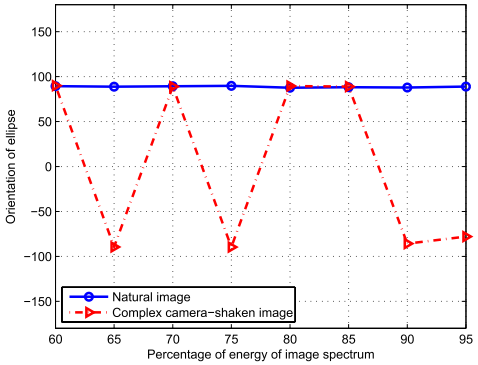

(b)

Fig. 6. (a) Examples of eccentricities and (b) orientations of ellipses that model the spectral contours of natural and complex camera-shaken images (from the CSI database).

The directional features capture changes in the orientation structure of the spectrum when an image is affected by motion blur caused by camera shake. Directional sharpness is captured by measurements of the variance and energy of the image spectrum across all (sampled) orientations. These are expected to decrease by generally different degrees in the direction of camera movement. Define the directional energy $DE(\phi_n)$ and the directional variance $DV(\phi_n)$ of the DFT coefficients as follows:

$$C_{\phi_n}(u) = \{B(u, u\tan(\phi_n)) \mid u \in (-N/2, N/2)\} \quad (3)$$

$$DE(\phi_n) = \left[\sum_{u=-N/2}^{N/2} \left|\frac{C_{\phi_n}(u)}{B(0,0)}\right|^2\right]^{-\frac{1}{2}} \quad (4)$$

$$f_{\phi_n}(u) = sgn(u) \cdot \frac{\sqrt{u^2 + u^2 \cdot \tan^2(u)}}{N} \quad (5)$$

$$DV(\phi_n) = \sum_{u=-N/2}^{N/2} p_{\phi_n}(u)\left[f_{\phi_n}(u) - \mu_{\phi_n}\right]^2 \quad (6)$$

where

$$p_{\phi_n}(u) = \frac{\left|C_{\phi_n}(u)\right|^2}{\sum_{u'=-N/2}^{N/2}\left|C_{\phi_n}(u')\right|^2}$$

$$\mu_{\phi_n} = \sum_{u=-N/2}^{N/2} p_{\phi_n}(u) f_{\phi_n}$$

where $B(u, v)$ is the DFT of the image and N is the DFT block size. $C_{\phi_n}(u)$ contains those image DFT coefficients that lie along the direction ϕ_n where $\phi_n \in \{\phi_1, \phi_2, \ldots, \phi_{N_{dr}}\}$ is the n^{th} sample of orientation and N_{dr} is the number of orientation samples. In addition, $p_{\phi_n}(u)$ is the probability mass function of the normalized power spectrum along each direction ϕ_n [23], μ_{ϕ_n} is the first central moment of the power spectrum along each direction ϕ_n, and $f_{\phi_n}(u)$ is normalized frequency, where $sgn(\cdot)$ is the sign function. We use linear interpolation to calculate those $u\tan(\phi_n)^{th}$ coefficients that do not fall on the discrete grid.

The directional sharpness $s(\phi_n)$ of the image along the direction ϕ_n is expressed as the product of $DE(\phi_n)$ and $DV(\phi_n)$.

$$s(\phi_n) = DE(\phi_n) \times DV(\phi_n) \quad (7)$$

We then define three features based on the directional sharpness feature (7) that quantify perceptual blur induced by camera shake. The first feature is the average directional sharpness:

$$F_1 = \mu_{s_\phi} = \frac{1}{N_{dr}}\sum_{n=1}^{N_{dr}} s(\phi_n). \quad (8)$$

In our implementation, we use $N_{dr} = 60$ equally spaced directions, hence $\phi_1 = 0°, \phi_2 = 3°, \ldots, \phi_{N_{dr}} = 177°$ [39].

The second directional feature is the CV of directional sharpness:

$$F_2 = \frac{\sigma_{s_\phi}}{\mu_{s_\phi}} \quad (9)$$

where

$$\sigma_{s_\phi} = \sqrt{\frac{1}{N_{dr}}\sum_{n=1}^{N_{dr}}\left[s(\phi_n) - \mu_{s_\phi}\right]^2}. \quad (10)$$

F_2 is close to 0 when the directional sharpness is identical in all directions, but it increases in the presence of highly directional, camera-shake induced blur of the image.

Finally, the third feature is the minimum directional sharpness:

$$F_3 = \min\left[s(\phi_n) | 1 \le n \le N_{dr}\right]. \quad (11)$$

F_3 captures the severity of the directional perceptual blur since oriented high frequency spectral coefficients are severely attenuated along the direction of camera motion.

Next, we define the shape based features that characterize the blur induced by camera shake in a different manner. Fig. 7 motivates the specific spectral shape features that provide additional discrimination power with regard to camera shake induced blur. The spectral shape features provide advantages over using the directional features alone, especially when the image content also has a directional nature. As described in Section III, we utilize ellipses to model the spectral contours of images in the DFT domain. Let N_{el} be the number of spectral contours and n be the index of the spectral contour. Let Γ_n denote the percentage of the energy of the DFT spectrum contained within contour $n+1$ but outside contour n, and Θ_n be the set of DFT coefficients lying within the $(n+1)^{st}$ spectral contour, but outside the n^{th} spectral contour.

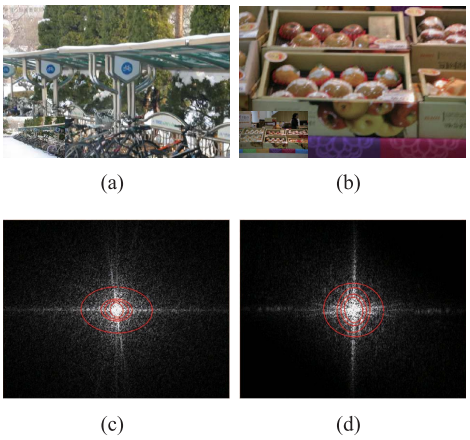

Fig. 7. Zooms of complex camera shaken images (a) MOS=3.93 and (b) MOS=2.57. The bottom-left of each image is an original version in each image. (c) The DFT spectrum of (a). (d) The DFT spectrum of (b). The spectral shape features provide additional discriminative power for measuring the sharpness of images (a) and (b), where, as in this example, the directional features may fail.

Further, let $\hat{B}$ denote the DFT coefficients B sorted in descending order so that $\hat{B}(k)$ is the k^{th} largest DFT coefficient. Then,

$$\Theta_n = \left\{ (u_k, v_k) | \Gamma_n \leq \frac{\sum_{k' < k} \hat{B}^2(k')}{\sum_v \sum_u B^2(u,v)} < \Gamma_{n+1}, \; 1 \leq k \leq N_W N_H \right\} \tag{12}$$

where N_W and N_H are the width and height of the image. We use fixed, evenly-spaced intervals of percentage of the energy $\Gamma_n = 0.60, 0.65, \ldots, 0.95, 1 \leq n \leq N_{el} + 1$ to define the contours [38]. Model parameters for the ellipses (major and minor axes and eccentricities) are obtained via least squares fitting on the DFT coefficients [40]. The ellipse model that we use is given by [41].

$$\frac{(u\cos\psi + v\sin\psi)^2}{c^2} + \frac{(u\sin\psi - v\cos\psi)^2}{d^2} = 1 \tag{13}$$

where c and d are the semi-major and semi-minor axes of the ellipse ($c \geq d$), and ψ is the orientation of the ellipse.

The first spectral shape feature (fourth overall) is the rate of increase of elliptical areas, denoted using F_4, as an indicator of perceptual blur:

$$F_4 = \left(\prod_{n=1}^{N_{el}-1} \frac{|A_n - A_{n+1}|}{A_n} \right)^{\frac{1}{N_{el}-1}} \tag{14}$$

where $A_n = \pi c_n d_n$ is the area of the n^{th} ellipse and c_n, d_n are the semi-major and semi-minor axes of the n^{th} spectral ellipse respectively.

We also utilize the eccentricity of each spectral ellipse, which indicates the degree by which the ellipse departs from circularity, as an indicator of perceptual blur. The eccentricity of the n^{th} ellipse is:

$$e_n = \sqrt{\frac{c_n^2 - d_n^2}{c_n^2}} = \sqrt{1 - \left(\frac{d_n}{c_n}\right)^2} \tag{15}$$

The second spectral shape feature (fifth overall) is the sample variance of the spectral eccentricities, which is expected to increase with the degree of camera shake induced blur:

$$F_5 = \frac{1}{N_{el}} \sum_{n=1}^{N_{el}} (e_n - \mu_e)^2 \tag{16}$$

where $\mu_e = \frac{1}{N_{el}} \sum_{n=1}^{N_{el}} e_n$ is the average eccentricity of the ellipses.

The last spectral shape feature uses the orientations of the spectral ellipses. Specifically, the sample variance of the spectral orientations, which is expected to increase with the degree of camera shake induced blur, is the third spectral shape feature (sixth overall):

$$F_6 = \frac{1}{N_{el}} \sum_{n=1}^{N_{el}} \left(\cos(\psi_n) - \mu_\psi\right)^2 \tag{17}$$

where $\mu_\psi = \frac{1}{N_{el}} \sum_{n=1}^{N_{el}} \cos(\psi_n)$ is the average orientation of the ellipses. We compute the cosine of the argument so that orientations of opposite polarities but similar orientation lead to similar measurements.

The learning process is defined in a straightforward manner. We use support vector regression (SVR) to predict the subjective sharpness scores using the six features (F_1 through F_6). The regression model is trained using an image quality database annotated by human opinion scores, as described in detail in Section VI-A. We used the libSVM package [42] using the linear kernel with parameters estimated by cross-validation to implement the SVR.

V. Camera-Shaken Image Database

To validate the performance of our algorithm, we built a test database called the Camera-Shaken Image (CSI) database and conducted a human study where we collected subjective sharpness assessment scores.

A. Test Stimuli

Test stimuli were acquired using a compact digital camera (Nikon COOLPIX P300) and a digital single-lens reflex (DSLR) camera (Canon EOS 5D) to represent 'casual' and 'high-performance' cameras, respectively. The image resolutions were 1024×768 and 1092×728 pixels, respectively. When the image resolution was larger than the display resolution, we downsampled the images using bicubic interpolation prior to display. To simulate typical motion blurs generated by naive users, we panned or shook the cameras by hand while acquiring the images. The database consists of two categories of distortion: linear and complex camera movement. Category I consists of 11 natural images and 99 blurred images afflicted by linear camera shake. The shaken images were acquired by manually panning the camera at three different ranges of speeds and in three different directions (horizontal, vertical and diagonal) using a hand-held camera. The apertures were varied between f/2.2–f/8, the exposure times varied between 1/40–1/30 sec, and the ISO was set to 160. Fig. 8 illustrates one of the linear shaken images in

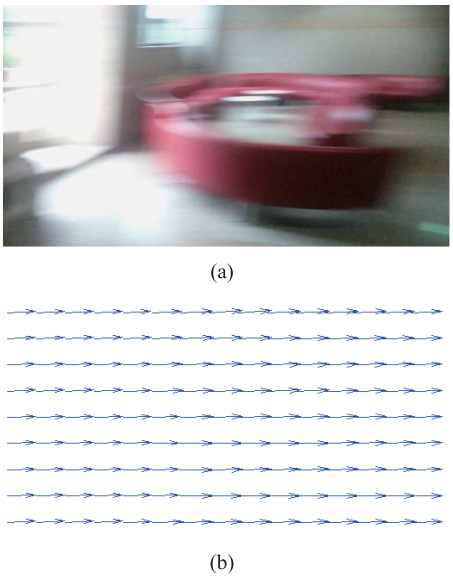

Fig. 8. (a) Linear camera shaken image with horizontal linear motion of the camera. (b) The local motion trajectories of (a) computed using an optical flow algorithm.

our database and its motion trajectories calculated using an optical flow algorithm [43]. Although it is difficult to control hand movement of the camera very precisely, Fig. 8 shows that the motion trajectory of the camera is horizontal and close to linear, as per design.

Category II consists of 25 naturalistic images impaired by complex camera movement caused by intentionally and manually shaking the camera during acquisition, also using three different ranges of intensity of camera shake. The apertures varied between f/3.5–f/32, the exposure times varied between 1/40–1 sec, and the ISO number varied between 100–800. Most of the stimuli were captured using an ISO setting of 160 (for Category I) and 100 (for Category II) to minimize the noise level.

B. Subjective Test

The test stimuli were displayed on an LG Electronics D2342P 23-inch liquid crystal display (LCD) monitor (1920×1080 at 60Hz), yielding a maximum luminance of 250 cd/m^2. The distance between the subject and the LCD monitor was held at about 85 cm which is three times the height of the display [44]. Twenty-three adults, aged between 23 and 30, took part in the experiment. We screened for visual acuity (Snellen test) and for color blindness (Ishihara test). After viewing the test image, the subjects rated their opinions of sharpness by drawing a slider on a sharpness scale. The sharpness scale was unlabelled numerically and divided into five equal portions, which were labelled with Likert marks ranging from "very annoying" through "imperceptible" following the ITU-R impairment scale [44]. The position of the slider was converted into a sharpness score by linearly mapping the entire scale to the interval [0 5] in floating point. To avoid subject fatigue, each participant rated images in 2 separate testing sessions, each having a duration of 20 minutes. A short training session was conducted whereby the subjects were instructed regarding the subjective test methodology using 10 training images. The training stimuli were captured using the same procedure as that of the test stimuli, but were not part of the CSI database. We selected the training stimuli to cover the same range of sharpness as the test stimuli in order to familiarize the subject with the range of sharpness they would be viewing in the study. We also made a playlist for the test session by shuffling the test stimuli in a random order. In order to prevent possible memory effects experienced when judging sharpness, the otherwise random arrangement of images presented to each subject excluded successive test stimuli that were obtained from the same reference image. This list was then divided equally into two sessions.

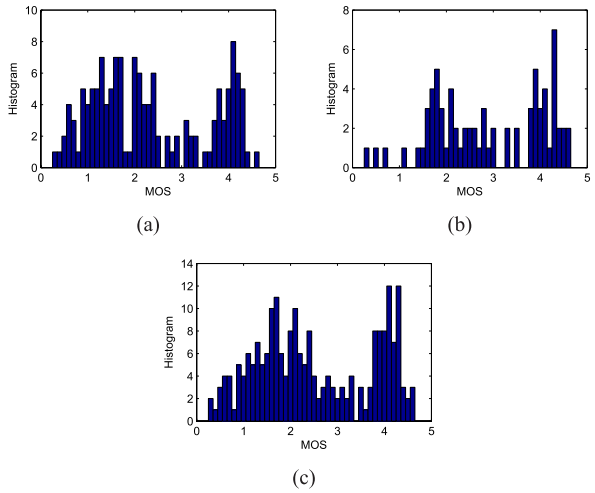

Fig. 9. Histogram of MOS from the CSI database. (a) Category I. (b) Category II. (c) Category I and II.

C. Processing of Subjective Scores

To analyze the subjective results, we processed the subjective scores and screened the recorded subjective scores to exclude those from unreliable subjects according to the guidelines described in ITU-R BT.500 [44]. Just one of the twenty-three subjects was rejected at this step.

Finally, the mean opinion score (MOS) of each image was calculated as the mean of scores from the remaining twenty-two subjects after subject rejection. Fig. 9 shows the histogram of the obtained MOS. For both blur categories I and II, the MOS were spread widely from 0 to 5.

VI. Performance

A. Performance Evaluation on CSI Database

To validate the performance of ISAC, we tested it on camera-shaken images from the CSI database. We used the Spearman rank order correlation coefficient (SROCC), the Pearson linear correlation coefficient (LCC) and the root mean squared prediction error (RMSE), as recommended by the video quality experts group (VQEG) [45]. A four parameter logistic function was used to fit algorithm scores to subjective scores [45]:

$$MOS_j = \frac{\beta_1 - \beta_2}{1 + e^{(S_j - \beta_3/|\beta_4|)}} + \beta_2 \tag{18}$$

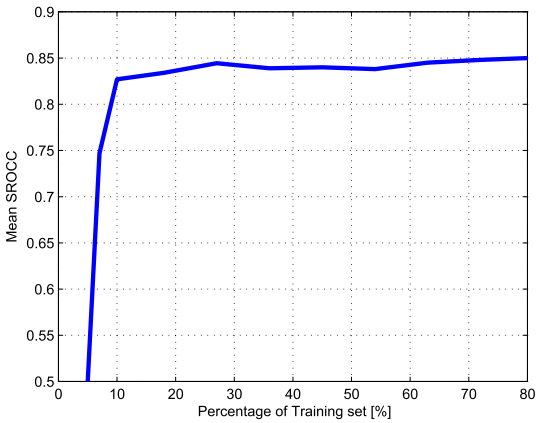

Fig. 10. Mean SROCC of ISAC as a function of the percentage of the CSI database used for training.

TABLE I
MEAN AND STANDARD DEVIATION OF SROCC AND LCC OF EACH FEATURE ACROSS 1000 TRAIN-TEST TRIALS ON THE CSI DATABASE

Feature	SROCC		LCC	
	Mean	std.dev.	Mean	std.dev.
F_1	0.8141	0.0417	0.8513	0.0390
F_2	0.6085	0.0866	0.6382	0.0779
F_3	0.7904	0.0539	0.8287	0.0545
F_4	0.7286	0.0513	0.7688	0.0557
F_5	0.6151	0.0807	0.6491	0.0743
F_6	0.1644	0.1235	0.1633	0.1041
F_1, F_2, F_3	0.8393	0.0473	0.8736	0.0393
F_4, F_5, F_6	0.7539	0.0574	0.7799	0.0562
F_1, F_2, F_3, F_4, F_5, F_6	0.8517	0.0367	0.8825	0.0311

where S_j is the sharpness score of the j^{th} image, and the model parameters $\beta_1, \beta_2, \beta_3$, and β_4 were obtained by minimizing the least square error between the MOS values and the fitted scores MOS_j.

The test and training sets input to the support vector regressor (SVR) were obtained from the CSI database by repeatedly and randomly subdividing it into two portions: 80% for training and the remaining 20% for testing, where the training and testing subsets do not share any image content. To verify that the results generalize across different training and test sets, we repeated the train-test sequence 1000 times using new randomly chosen training and testing sets at each iteration. We then evaluated the mean SROCC across 1000 trials as shown in Fig. 10. We also repeated this entire process across a wide range of content percent divisions. The percentage comprised by the training set was varied from 5% to 80%. It was observed that the average SROCC stabilized above 0.82 when only 10% of the data was used for training.

Table I shows the mean and standard deviation of SROCC and LCC for each of the six features across 1000 train-test trials. We also show the performance of the combination of directional features and shape based features. Each feature contributes to the overall evaluation of perceptual blur and the combination of all features improves upon the individual features.

TABLE II
MEAN SPEARMAN RANK ORDERED CORRELATION COEFFICIENT (SROCC) AND STANDARD DEVIATION ACROSS 1000 TRAIN-TEST TRIALS ON THE CSI DATABASE

	Category I		Category II		All	
	Mean	std.dev.	Mean	std.dev.	Mean	std.dev.
M1	0.6352	0.0482	0.7098	0.2757	0.6922	0.0190
M2	0.5128	0.0830	0.7050	0.0305	0.5814	0.0529
M3	0.6905	0.0270	0.7177	0.0421	0.7109	0.0207
M4	0.2998	0.0943	0.4856	0.0506	0.3648	0.0461
M5	0.5819	0.0465	0.2242	0.0945	0.4387	0.0354
M6	0.6800	0.0499	0.5489	0.0402	0.6616	0.0417
M7	0.8128	0.0582	0.7868	0.0958	0.8181	0.0495
M8	0.8386	0.0626	**0.7953**	0.0868	0.8393	0.0473
M9	0.7932	0.0657	0.6659	0.1166	0.7539	0.0574
M10	**0.8585**	0.0412	0.7886	0.0774	**0.8517**	0.0367

TABLE III
MEAN LINEAR CORRELATION (LCC) AND STANDARD DEVIATION ACROSS 1000 TRAIN-TEST TRIALS ON THE CSI DATABASE

	Category I		Category II		All	
	Mean	std.dev.	Mean	std.dev.	Mean	std.dev.
M1	0.7477	0.0326	0.7365	0.2657	0.7562	0.0221
M2	0.5699	0.0607	0.7507	0.0233	0.6459	0.0369
M3	0.7700	0.0322	0.7424	0.0268	0.7540	0.0171
M4	0.2845	0.0615	0.5061	0.0572	0.3421	0.0536
M5	0.6207	0.0603	0.1936	0.1188	0.4639	0.0488
M6	0.7227	0.0651	0.5578	0.0467	0.6704	0.0599
M7	0.8837	0.0469	0.8214	0.0906	0.8554	0.0440
M8	0.9152	0.0330	**0.8322**	0.0886	0.8736	0.0393
M9	0.8279	0.0596	0.7083	0.1126	0.7799	0.0562
M10	**0.9230**	0.0246	0.8197	0.0764	**0.8825**	0.0311

TABLE IV
MEAN ROOT MEAN SQUARE ERROR (RMSE) AND STANDARD DEVIATION ACROSS 1000 TRAIN-TEST TRIALS ON THE CSI DATABASE

	Category I		Category II		All	
	Mean	std.dev.	Mean	std.dev.	Mean	std.dev.
M1	0.8116	0.0439	0.7218	0.0917	0.7986	0.0301
M2	0.9896	0.0560	0.7543	0.0409	0.9314	0.0409
M3	0.7737	0.0574	0.7648	0.0427	0.8023	0.0300
M4	1.1617	0.0382	0.9829	0.0452	1.1467	0.0293
M5	0.9423	0.0770	1.1139	0.0393	1.0810	0.0392
M6	0.8339	0.0877	0.9465	0.0399	0.9063	0.0542
M7	0.5569	0.1071	**0.6176**	0.1351	0.6245	0.0930
M8	0.4801	0.0948	0.6568	0.1416	0.5875	0.0944
M9	0.6657	0.0925	0.7737	0.1440	0.7555	0.0765
M10	**0.4602**	0.0657	0.6272	0.1265	**0.5688**	0.0726

Tables II–IV show the means and standard deviations of SROCC, LCC and RMSE across the 1000 train-test trials. We deployed three versions of our blur prediction model: ISAC-D and ISAC-S use only the directional or shape features respectively. ISAC utilizes both types of features. To compare the performance of ISAC against the state-of-the-art, we also evaluated the performance of Marziliano [18], JNBM [1], CPBD [19], Zhang [22], Caviedes [23], DIIVINE [24] and S3 [46]. M1 through M10 are Marziliano, JNBM, CPBD,

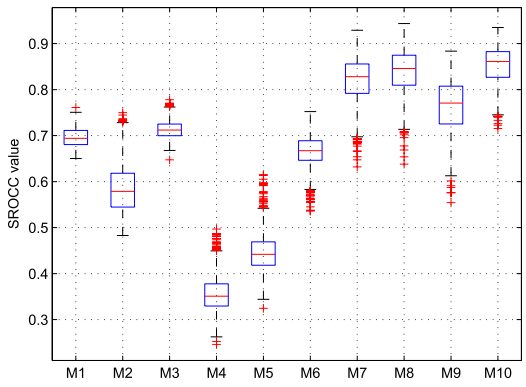

(a)

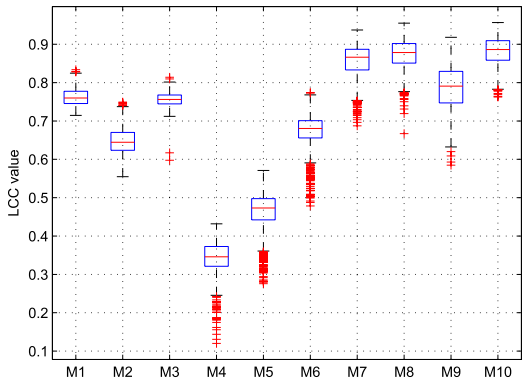

(b)

Fig. 11. Box plots expressing the performance distributions of the various blur prediction algorithms across 1000 train-test trials on Category I and II blurs. (a) SROCC. (b) LCC.

Zhang, Caviedes, DIIVINE, S3, ISAC-D, ISAC-S and ISAC respectively. ISAC-D and ISAC-S delivered better predictive performance than all of the other algorithms. This indicates that the ISAC spectral features are highly effective for predicting the loss of sharpness of camera-shaken images. Further, ISAC performed better than both ISAC-D and ISAC-S. ISAC captures spectral variation along both orientations and radial spatial frequency bands. Fig. 11 shows plots of SROCC and LCC computed over 1000 experimental trials. The plots show that the ISAC models are statistically superior to the existing models in terms of SROCC and LCC.

B. Statistical Significance of Results on CSI Database

In addition, we tested the statistical significance of the performance of each model. The residual error between the quality prediction of an objective model and the MOS values on the CSI Database can be used to test the statistical superiority of one model over another. The F-test was performed on the ratio of the variance of the residual error from one objective model to that of another objective model [47], [48]. The F-test assumes that the residuals are normally distributed and we tested this assumption by performing the Jarque-Bera (JB) test [49], [50]. Table V shows the results of the JB-test for a significance level of 5%. The results show that the distribution of the residuals of all objective models are normal, thus validating the use of the F-test.

TABLE V

RESULTS OF JB-TEST PERFORMED ON THE RESIDUALS BETWEEN MODEL PREDICTIONS AND MOS VALUES. THE LAST COLUMN SHOWS THE TEST DECISION FOR A SIGNIFICANCE LEVEL OF 5%. A SYMBOL VALUE OF "1" INDICATES THAT THE NULL HYPOTHESIS IS ACCEPTED AND THE RESIDUALS ARE NORMALLY DISTRIBUTED. EACH ENTRY IN THE TABLE IS A CODEWORD CONSISTING OF THREE SYMBOLS. THE SYMBOLS CORRESPOND TO "CATEGORY I", "CATEGORY II" AND "ALL" IN THAT ORDER

	JB statistic			Test Decision
	Category I	Category II	All	
M1	2.6056	1.0607	3.7541	1 1 1
M2	3.8014	1.2162	4.2897	1 1 1
M3	1.4067	0.9928	1.3251	1 1 1
M4	2.5531	0.9501	2.9859	1 1 1
M5	1.8088	0.9978	1.7807	1 1 1
M6	1.6738	1.0223	1.6056	1 1 1
M7	1.1676	0.9415	1.3662	1 1 1
M8	1.1601	0.9783	1.9363	1 1 1
M9	2.3535	0.8535	2.5157	1 1 1
M10	1.0553	0.6829	1.9086	1 1 1

Table VI shows the results of the F-test. A symbol value of "1" ("0") indicates that the statistical performance of the model in the row is superior (inferior) to that of the model in the column. A symbol value of "-" indicates that the statistical performance of the model in the row is equivalent to that of the model in the column. As before, M1 through M10 are Marziliano, JNMB, CPBD, Zhang, Caviedes, DIIVINE, S3, ISAC-D, ISAC-S and ISAC respectively. The results indicate that ISAC-D, ISAC-S and ISAC achieve better performance than all of the existing models with statistical significance. Furthermore, both ISAC-D and ISAC are statistically better than all other algorithms on Category I blur. Clearly, oriented features are better able to capture directional variations of image spectral induced by linear shake.

C. Performance Evaluation on an Independent Database

Finally, as independent verification, we also tested ISAC on another existing (albeit much smaller) camera-shaken image database [51]. This database contains four natural images of 800×800 resolution captured using a Canon EOS 5D Mark II camera. 12 blurred images were generated from these natural images using linear and complex camera shake patterns that were simulated by moving the camera using a mechanical device. This database is complementary to our own in that the camera motions are precise and controlled, even if they less realistically represent camera movements caused by casual human users. Since this database does not include subjective sharpness scores, we conducted a subjective study on the

TABLE VI
RESULTS OF F-TEST PERFORMED ON THE RESIDUALS BETWEEN MODEL PREDICTIONS AND MOS VALUES. EACH ENTRY IN THE TABLE IS A CODEWORD CONSISTING OF THREE SYMBOLS. THE SYMBOLS CORRESPOND TO "CATEGORY I", "CATEGORY II" AND "ALL" IN THAT ORDER

	M1	M2	M3	M4	M5	M6	M7	M8	M9	M10
M1	- - -	1 - 1	- - -	1 1 1	1 1 1	- 1 1	0 - -	0 - -	- - -	0 - 0
M2	0 - 0	- - -	0 - 0	1 1 1	- 1 1	0 1 -	0 - 0	0 - 0	0 - -	0 - 0
M3	- - -	1 - 1	- - -	1 1 1	1 1 1	- 1 1	0 - -	0 - 0	- - -	0 - 0
M4	0 0 0	0 0 0	0 0 0	- - -	0 - -	0 - 0	0 - 0	0 - 0	0 - 0	0 - 0
M5	0 0 0	- 0 0	0 0 0	1 - -	- - -	- - -	0 0 0	0 0 0	0 - 0	0 0 0
M6	- 0 0	1 0 -	- 0 0	1 - 1	- - -	- - -	0 - 0	0 - 0	- - 0	0 - 0
M7	1 - -	1 - 1	1 - -	1 - 1	1 1 1	1 - 1	- - -	- - -	1 - 1	- - -
M8	1 - -	1 - 1	1 - 1	1 - 1	1 1 1	1 - 1	- - -	- - -	1 - 1	- - -
M9	- - -	1 - -	- - -	1 - 1	1 - 1	- - 1	0 - 0	0 - 0	- - -	0 - 0
M10	1 - 1	1 - 1	1 - 1	1 - 1	1 1 1	1 - 1	- - -	- - -	1 - 1	- - -

TABLE VII
SROCC, LCC AND RMSE RESULTS OBTAINED BY TRAINING ON THE CSI DATABASE AND TESTING ON THE DATABASE [51]

	SROCC	LCC	RMSE
Marziliano [18]	0.1937	0.2607	1.1217
JNBM [1]	0.5077	0.4864	0.9827
CPBD [19]	0.3656	0.5044	1.0033
Zhang [22]	0.5894	0.6484	0.8846
Caviedes [23]	0.5262	0.2158	1.1349
DIIVINE [24]	0.5264	0.4229	1.0192
S3 [46]	0.8577	0.8962	0.4990
ISAC-D	0.7957	0.8459	0.5999
ISAC-S	0.6124	0.7358	0.7616
ISAC	**0.8367**	**0.8829**	**0.5281**

database using 8 subjects, by following the same procedure as described in Section V.

We evaluated ISAC on the database described in [51] after training the SVR model parameters on the entire CSI database. The performance of ISAC may again be seen to be highly competitive relative to the other compared models as indicated by the SROCC, LCC and RMSE scores reported in Table VII. The competitive performance of ISAC on the database [51], even though trained on the very different CSI database, nicely illustrates its generalized camera shake induced blur predictive power.

VII. CONCLUSION

We have described a new Image Sharpness Assessment model for Camera-Shaken Images (ISAC) that utilizes statistical measures of the spectra of camera-shaken images. Most previous approaches have been designed to detect quality degradations arising from defocus blur, whereas ISAC is specifically designed to predict perceptual distortions induced by camera shake. ISAC predicts perceivable sharpness degradations by combining spectral directional and shape features. SVR was used to regress on these features against subjective scores to develop an algorithm to predict perceptual blur. To verify the performance of ISAC, we constructed a camera-shaken image database that includes linear and complex camera movements along with subjective test results. We demonstrated that the ISAC model predicts sharpness degradations on camera-shaken images more accurately than existing no-reference image blur prediction and quality assessment models.

In the future, we would like to study the performance of ISAC on large databases of videos acquired by real world users on different cameras that suffer from motion blur. Also, the ISAC algorithm assumes that the entire image is blurred due to camera shake and is not designed to handle images with local blur - as an example, out-of-focus blur created due to a camera's shallow depth of field. In the future, we would like to extend the ISAC model to handle these types of local blurs.

REFERENCES

[1] R. Ferzli and L. J. Karam, "A no-reference objective image sharpness metric based on the notion of just noticeable blur (JNB)," *IEEE Trans. Image Process.*, vol. 18, no. 4, pp. 717–728, Apr. 2009.
[2] R. Hassen, Z. Wang, and M. Salama, "No-reference image sharpness assessment based on local phase coherence measurement," in *Proc. IEEE Int. Conf. Acoust. Speech Signal Process.*, Mar. 2010, pp. 2434–2437.
[3] H. J. Trussell and S. Fogel, "Identification and restoration of spatially variant motion blurs in sequential images," *IEEE Trans. Image Process.*, vol. 1, no. 1, pp. 123–126, Jan. 1992.
[4] M. Ben-Ezra and S. K. Nayar, "Motion-based motion deblurring," *IEEE Trans. Pattern Anal. Mach. Intell.*, vol. 26, no. 6, pp. 689–698, Jun. 2004.
[5] T. S. Cho, A. Levin, F. Durand, and W. T. Freeman, "Motion blur removal with orthogonal parabolic exposures," in *Proc. IEEE Int. Conf. Comput. Photogr.*, Mar. 2010, pp. 1–8.
[6] Y. Qian, Y. Li, J. Shao, and H. Miao, "Real-time image stabilization for arbitrary motion blurred image based on opto-electronic hybrid joint transform correlator," *Opt. Exp.*, vol. 19, no. 11, pp. 10762–10768, May 2011.
[7] M. Song *et al.*, "Development of small sized actuator with compliant mechanism for optical image stabilization," *IEEE Trans. Magn.*, vol. 46, no. 6, pp. 2369–2372, Jun. 2010.
[8] S. Cho and S. Lee, "Fast motion deblurring," *ACM Trans. Graph.*, vol. 28, no. 5, pp. 145:1–145:8, Dec. 2009.
[9] H. R. Sheikh, A. C. Bovik, and L. Cormack, "No-reference quality assessment using natural scene statistics: JPEG2000," *IEEE Trans. Image Process.*, vol. 14, no. 11, pp. 1918–1927, Nov. 2005.
[10] S. Lee, M. S. Pattichis, and A. C. Bovik, "Foveated video compression with optimal rate control," *IEEE Trans. Image Process.*, vol. 10, no. 7, pp. 977–992, Jul. 2001.
[11] T. Oh and S. Lee, "Implementation of multimode-multilevel block truncation coding for LCD overdrive," *IEICE Trans. Fundam. Electron., Commun. Comput. Sci.*, vol. 95, no. 5, pp. 867–875, 2012.
[12] J. Park, H. Lee, S. Lee, and A. C. Bovik, "Optimal channel adaptation of scalable video over a multicarrier-based multicell environment," *IEEE Trans. Multimedia*, vol. 11, no. 6, pp. 1062–1071, Oct. 2009.

[13] T. Oh, H. Lee, and S. Lee, "Dynamic bandwidth and carrier allocation for video broadcast/multicast over multi-cell environments," *Wireless Pers. Commun.*, Apr. 2013, pp. 1–21.
[14] T. Oh and S. Lee, "Cooperative and joint video multicast over MIMO–OFDM networks," *Digital Signal Process.*, vol. 33, pp. 98–115, Oct. 2014.
[15] L. Liang, S. Wang, J. Chen, S. Ma, D. Zhao, and W. Gao, "No-reference perceptual image quality metric using gradient profiles for JPEG2000," *Signal Process., Image Commun.*, vol. 25, pp. 502–516, Aug. 2010.
[16] J. Elder and S. Zucker, "Local scale control for edge detection and blur estimation," *IEEE Trans. Pattern Anal. Mach. Intell.*, vol. 20, no. 7, pp. 699–716, Jul. 1998.
[17] H. Hu and G. de Haan, "Low cost robust blur estimator," in *Proc. IEEE Int. Conf. Image Process.*, Oct. 2006, pp. 617–620.
[18] P. Marziliano, F. Dufaux, S. Winkler, and T. Ebrahimi, "A no-reference perceptual blur metric," in *Proc. IEEE Int. Conf. Image Process.*, vol. 3. Nov. 2002, pp. 57–60.
[19] N. D. Narvekar and L. J. Karam, "A no-reference image blur metric based on the cumulative probability of blur detection (CPBD)," *IEEE Trans. Image Process.*, vol. 20, no. 9, pp. 2678–2683, Sep. 2011.
[20] N. G. Sadaka, L. J. Karam, R. Ferzli, and G. P. Abousleman, "A no-reference perceptual image sharpness metric based on saliency-weighted foveal pooling," in *Proc. 15th IEEE Int. Conf. Image Process.*, Oct. 2008, pp. 369–372.
[21] X. Marichal, W.-Y. Ma, and H. Zhang, "Blur determination in the compressed domain using DCT information," in *Proc. IEEE Int. Conf. Image Process.*, vol. 2. Oct. 1999, pp. 386–390.
[22] N. F. Zhang, M. T. Postek, R. D. Larrabee, A. E. Vladar, W. J. Keery, and S. N. Jones, "Image sharpness measurement in the scanning electron-microscope—Part III," *J. Scanning Microsc.*, vol. 21, no. 4, pp. 246–252, Jul. 1999.
[23] J. Caviedes and F. Oberti, "A new sharpness metric based on local kurtosis, edge and energy information," *Signal Process., Image Commun.*, vol. 19, no. 2, pp. 147–161, 2004.
[24] A. K. Moorthy and A. C. Bovik, "Blind image quality assessment: From natural scene statistics to perceptual quality," *IEEE Trans. Image Process.*, vol. 20, no. 12, pp. 3350–3364, Dec. 2011.
[25] M. Saad, A. Bovik, and C. Charrier, "Blind image quality assessment: A natural scene statistics approach in the DCT domain," *IEEE Trans. Image Process.*, vol. 21, no. 8, pp. 3339–3352, Aug. 2012.
[26] H. Tang, N. Joshi, and A. Kapoor, "Learning a blind measure of perceptual image quality," in *Proc. IEEE Conf. Comput. Vis. Pattern Recognit.*, Jun. 2011, pp. 305–312.
[27] A. E. Savakis and H. J. Trussell, "Blur identification by residual spectral matching," *IEEE Trans. Image Process.*, vol. 2, no. 2, pp. 141–151, Apr. 1993.
[28] L. Xu and J. Jia, "Two-phase kernel estimation for robust motion deblurring," in *Proc. 11th IEEE Euro. Conf. Comput. Vis.*, Sep. 2010, pp. 157–170.
[29] M. E. Moghaddam and M. Jamzad, "Motion blur identification in noisy images using mathematical models and statistical measures," *Pattern Recognit.*, vol. 40, no. 7, pp. 1946–1957, Jul. 2007.
[30] T. S. Cho, S. Paris, B. K. P. Horn, and W. T. Freeman, "Blur kernel estimation using the radon transform," in *Proc. IEEE Conf. Comput. Vis. Pattern Recognit.*, Jun. 2011, pp. 241–248.
[31] D. C. Burr and M. J. Morgan, "Motion deblurring in human vision," *Proc. Roy. Soc. Ser. B, Biol. Sci.*, vol. 264, no. 1380, pp. 431–436, 1997.
[32] S. T. Hammett, "Motion blur and motion sharpening in the human visual system," *Vis. Res.*, vol. 37, no. 18, pp. 2505–2510, Sep. 1997.
[33] S. T. Hammett, M. A. Georgeson, and A. Gorea, "Motion blur and motion sharpening: Temporal smear and local contrast non-linearity," *Vis. Res.*, vol. 38, no. 14, pp. 2099–2108, Jul. 1998.
[34] P. J. Bex, G. K. Edgar, and A. T. Smith, "Sharpening of drifting, blurred images," *Vis. Res.*, vol. 35, no. 18, pp. 2539–2546, Sep. 1995.
[35] G. M. Johnson and M. D. Fairchild, "Sharpness rules," in *Proc. 8th Color Imag. Conf.*, 2000, pp. 24–30.
[36] H.-Y. Lin and K.-J. Li, "Motion blur removal and its application to vehicle speed detection," in *Proc. IEEE Int. Conf. Image Process.*, vol. 5. Oct. 2004, pp. 3407–3410.
[37] F. Brusius, U. Schwanecke, and P. Barth, "Blind image deconvolution of linear motion blur," in *Computer Vision, Imaging and Computer Graphics. Theory and Applications*. Berlin, Germany: Springer-Verlag, 2013, pp. 105–119.
[38] A. Torralba and A. Oliva, "Statistics of natural image categories," *Network*, vol. 14, no. 3, pp. 391–412, 2003.
[39] A. van der Schaaf and J. H. van Hateren, "Modelling the power spectra of natural images: Statistics and information," *Vis. Res.*, vol. 36, no. 17, pp. 2759–2770, Sep. 1996.
[40] M. Pilu, A. W. Fitzgibbon, and R. B. Fisher, "Ellipse-specific direct least-square fitting," in *Proc. Int. Conf. Image Process.*, vol. 3. Sep. 1996, pp. 599–602.
[41] D. Kalman, "The most marvelous theorem in mathematics," *J. Online Math. Appl.*, vol. 8, 2008.
[42] C.-C. Chang and C.-J. Lin, "LIBSVM: A library for support vector machines," *ACM Trans. Intell. Syst. Technol.*, vol. 2, no. 3, 2001, Art. ID 27.
[43] D. Sun, S. Roth, and M. J. Black, "Secrets of optical flow estimation and their principles," in *Proc. IEEE Conf. Comput. Vis. Pattern Recognit.*, Jun. 2010, pp. 2432–2439.
[44] *Methodology for the Subjective Assessment of the Quality of Television Pictures*, document ITU-R BT.500-11, 2000.
[45] *Final Report From the Video Quality Experts Group on the Validation of Objective Models of Video Quality Assessment*, VQEG, Boulder, CO, USA, Mar. 2000.
[46] C. T. Vu, T. D. Phan, and D. M. Chandler, "S_3: A spectral and spatial measure of local perceived sharpness in natural images," *IEEE Trans. Image Process.*, vol. 21, no. 3, pp. 937–945, Mar. 2012.
[47] K. Seshadrinathan, R. Soundararajan, A. C. Bovik, and L. K. Cormack, "Study of subjective and objective quality assessment of video," *IEEE Trans. Image Process.*, vol. 19, no. 8, pp. 1427–1441, Jun. 2010.
[48] J. Park, K. Seshadrinathan, S. Lee, and A. C. Bovik, "Video quality pooling adaptive to perceptual distortion severity," *IEEE Trans. Image Process.*, vol. 22, no. 2, pp. 610–620, Feb. 2013.
[49] G. E. P. Box, "Non-normality and tests on variances," *Biometrika*, vol. 40, nos. 3–4, pp. 318–335, 1953.
[50] C. M. Jarque and A. K. Bera, "Efficient tests for normality, homoscedasticity and serial independence of regression residuals," *Econ. Lett.*, vol. 6, no. 3, pp. 255–259, 1980.
[51] R. Kohler, M. Hirsch, B. Mohler, B. Scholkopf, and S. Harmeling, "Recording and playback of camera shake: Benchmarking blind deconvolution with a real-world database," in *Proc. IEEE 12th Eur. Conf. Comput. Vis.*, Oct. 2012, pp. 27–40.

Taegeun Oh was born in Korea in 1984. He received the B.S. and Ph.D. degrees in electrical and electronic engineering from Yonsei University, Seoul, Korea, in 2007 and 2014, respectively. He has been with the Agency for Defense Development, Daejeon, Korea, since 2014. His research interests include image/video quality assessments, image/video coding, and multimedia communications.

Jincheol Park was born in Korea in 1982. He received the B.S. degree in information and electronic engineering from Soongsil University, Seoul, Korea, in 2006, and the M.S. and Ph.D. degrees in electrical and electronic engineering from Yonsei University, Seoul, in 2008 and 2013, respectively. He was a Visiting Researcher with the Laboratory for Image and Video Engineering, Department of Electrical and Computer Engineering, University of Texas at Austin, Austin, TX, USA, from 2010 to 2011. His current research interests include 2D and 3D video quality assessment.

Kalpana Seshadrinathan (S'03–M'09) received the B.Tech. degree from the University of Kerala, Thiruvananthapuram, India, in 2002, and the M.S. and Ph.D. degrees in electrical engineering from the University of Texas at Austin, Austin, TX, USA, in 2004 and 2008, respectively. She is currently a System Engineer with Intel Corporation, Chandler, AZ, USA. Her research interests include image and video quality assessment, computational aspects of human vision, motion estimation and its applications, and statistical modeling of images and video. She was an Assistant Director of the Laboratory for Image and Video Engineering with the University of Texas at Austin from 2005 to 2008. She was a recipient of the 2003 Texas Telecommunications Engineering Consortium Graduate Fellowship Award and the 2007 Graduate Student Professional Development Award from the University of Texas at Austin.

Sanghoon Lee (M'05–SM'12) received the B.S. degree in electrical engineering from Yonsei University, Seoul, Korea, in 1989, and the M.S. degree in electrical engineering from the Korea Advanced Institute of Science and Technology, Daejeon, Korea, in 1991. From 1991 to 1996, he was with Korea Telecom, Seongnam, Korea. He received the Ph.D. degree in electrical engineering from the University of Texas at Austin, Austin, TX, USA, in 2000. From 1999 to 2002, he was with Lucent Technologies, Inc., Murray Hill, NJ, USA, where he was involved in 3G wireless and multimedia networks. In 2003, he joined the faculty of the Department of Electrical and Electronics Engineering with Yonsei University, where he is currently a Full Professor. He was an Associate Editor of the IEEE TRANSACTIONS ON IMAGE PROCESSING (2010–2014). He has been an Associate Editor of the IEEE SIGNAL PROCESSING LETTERS (2014-), an Editor of the *Journal of Communications and Networks* (2009-), and the Chair of the IEEE P3333.1 Quality Assessment Working Group (2011-). He served as the Technical Committee Member of the IEEE Image, Video, and Multidimensional Signal Processing (IVMSP) (2014-), the Technical Program Co-Chair of the International Conference on Information Networking (2014), the Global 3D Forum (2012, 2013), the General Chair of the IEEE IVMSP Workshop (2013), and the Guest Editor of the IEEE TRANSACTIONS ON IMAGE PROCESSING (2013). He has received the Special Service Award from the IEEE Broadcast Technology Society (2012) and the IEEE Signal Processing Society (2013). His research interests include image/video quality assessments, medical image processing, cloud computing, wireless multimedia communications, and wireless networks.

Alan Conrad Bovik (S'80–M'81–SM'89–F'96) is currently the Curry/Cullen Trust Endowed Chair Professor with the University of Texas at Austin, Austin, TX, USA, where he is also the Director of the Laboratory for Image and Video Engineering, and a faculty member with the Department of Electrical and Computer Engineering and the Center for Perceptual Systems, Institute for Neuroscience. His research interests include image and video processing, computational vision, and visual perception. He has authored over 650 technical articles in these areas and holds two U.S. patents. His several books include the recent companion volumes *The Essential Guides to Image and Video Processing* (Academic Press, 2009).

He was a recipient of a number of major awards from the IEEE Signal Processing Society, including the Best Paper Award (2009), the Education Award (2007), the Technical Achievement Award (2005), and the Meritorious Service Award (1998). He was also a recipient of the Honorary Member Award from the Society for Imaging Science and Technology (2013), the Society of Photo-Optical and Instrumentation Engineers (SPIE) Technology Achievement Award (2012), and the IS&T/SPIE Imaging Scientist of the Year Award (2011). He received the Hocott Award for Distinguished Engineering Research at the University of Texas at Austin. He was a recipient of the Distinguished Alumni Award from the University of Illinois at Urbana-Champaign (2008), the IEEE Third Millennium Medal (2000), and two Journal Paper Awards from the International Pattern Recognition Society (1988 and 1993). He is a fellow of the Optical Society of America, SPIE, and the American Institute of Medical and Biomedical Engineering. He has been involved in numerous professional society activities, including the Board of Governors of the IEEE Signal Processing Society (1996–1998), the Co-Founder and Editor-in-Chief of the IEEE TRANSACTIONS ON IMAGE PROCESSING (1996–2002), an Editorial Board Member of the PROCEEDINGS OF THE IEEE (1998–2004), a Series Editor of the *Image, Video, and Multimedia Processing* (Morgan and Claypool Publisher, 2003–present), and the Founding General Chairman of the First IEEE International Conference on Image Processing in Austin (1994).

Dr. Bovik is a registered Professional Engineer in the state of Texas, and a Frequent Consultant to legal, industrial, and academic institutions.